Synthesis, disorder and Ising anisotropy in a new spin liquid candidate PrMgAl$_{11}$O$_{19}$

Yantao Cao[1,2] , **Huanpeng Bu**[2]**, Zhendong Fu**[2]**, Jinkui Zhao**[2,3]**, Jason S Gardner**[4,*]**, Zhongwen Ouyang**[5]**, Zhaoming Tian**[5,*]**, Zhiwei Li**[1,*] **and Hanjie Guo**[2,*]

[1] Key Lab for Magnetism and Magnetic Materials of the Ministry of Education, Lanzhou University, Lanzhou 730000, People's Republic of China
[2] Songshan Lake Materials Laboratory, Dongguan, Guangdong 523808, People's Republic of China
[3] Institute of Physics, Chinese Academy of Sciences, Beijing 100190, People's Republic of China
[4] Materials Science and Technology Division, Oak Ridge National Laboratory, Oak Ridge, TN 37831, United States of America
[5] School of Physics and Wuhan National High Magnetic Field Center, Huazhong University of Science and Technology, Wuhan 430074, People's Republic of China

E-mail: gardnerjs@ornl.gov, tianzhaoming@hust.edu.cn, zweili@lzu.edu.cn and hjguo@sslab.org.cn

Abstract

Here we report the successful synthesis of large single crystals of triangular frustrated PrMgAl$_{11}$O$_{19}$ using the optical floating zone technique. Single crystal x-ray diffraction (XRD) measurements unveiled the presence of quenched disorder within the mirror plane, specifically ~7% of Pr ions deviating from the ideal $2d$ site towards the $6h$ site. Magnetic susceptibility measurements revealed an Ising anisotropy with the c-axis being the easy axis. Despite a large spin–spin interaction that develops below ~10 K and considerable site disorder, the spins do not order or freeze down to at least 50 mK. The availability of large single crystals offers a distinct opportunity to investigate the exotic magnetic state on a triangular lattice with an easy axis out of the plane.

Supplementary material for this article is available online

Keywords: spin liquid, disorder, frustration, triangular lattice, Ising anisotropy

Introduction

Quantum spin liquids (QSLs) represent an intriguing state where the spins remain disordered even at zero Kelvin due to quantum fluctuations, albeit with strong spin–spin couplings [1]. Achieving a QSL ground state is challenging because of

the propensity for the spin sublattice to freeze as the temperature is lowered, especially around defects and/or disorder which act as pinning centers. For example, in the triangular lattice of YbMgGaO$_4$, the presence of site disorder between the nonmagnetic ions Mg and Ga induces a spin glass behavior [2]. However, disorder is not always detrimental to the QSL state. Studies on the pyrochlore oxides [3, 4] and 1T-TaS$_2$ [5] reveal that the quenched disorder does not compete, but rather cooperates with the frustration to induce strong quantum fluctuations, and may give rise to emergent spin disordered state responsible for the gapless excitations.

From an experimental point of view, a QSL state does not break any symmetry making it arduous to identify using a single technique [6]. Inelastic neutron scattering plays an
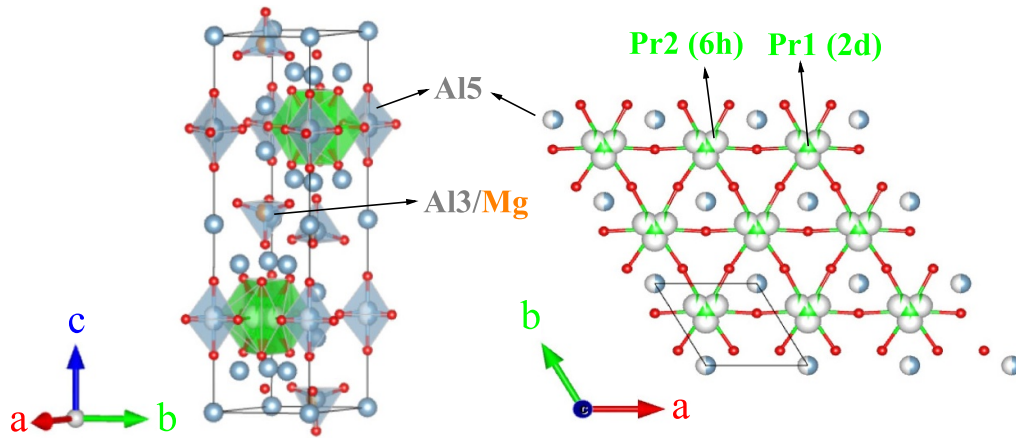

1

Figure 1. The crystal structure of $PrMgAl_{11}O_{19}$ extracted from single-crystal XRD refinement. Green—Pr; grey—Al; red—O; orange—Mg. The mirror plane including the disordered Pr ions is depicted in the right panel.

important role in providing crucial evidence for a QSL state, as fractional excitations, such as spinons, manifest as a distinctive excitation continuum in the spectrum [7]. The availability of high-quality large single crystals is essential for neutron scattering due to the small scattering cross-section and low neutron flux. Similar requisites hold true for other measurements, such as spin thermal transport, to minimize any grain boundary effects as well as the anisotropic characterizations of magnetic behaviors [8, 9].

Here we present the single crystal growth of a hexaaluminate, $PrMgAl_{11}O_{19}$, using the optical floating zone technique. Crystal growth and basic magnetic property measurements on this series of lanthanide aluminates have been reported [10, 11], but a detailed characterization down to milikelvin is still lacking. Our previous results on the isostructural, polycrystalline $PrZnAl_{11}O_{19}$ already suggested the magnetic sublattice of Pr^{3+} ions, decorating a triangular lattice, has the potential to host a Dirac QSL [12, 13]. The triangular network of Pr ions reside within the *ab* plane, and are connected via intermediate O ions which are also within the triangular plane, forming a nearly linear Pr–O–Pr bond with an angle of about 176.7°. These layers are separated along the *c*-axis by ~11 Å while the nearest neighbor Pr–Pr bond is ~5.59 Å; see figure 1. As a comparison, the distance between triangular layers in $YbMgGaO_4$ are about 8 Å with a nearest neighbor bond length of ~3.40 Å [14]. Moreover, the large difference in the ionic radii between the magnetic and nonmagnetic ions inhibits any site mixing between the magnetic and nonmagnetic ions. These structural features indicate that this system is an ideal quasi-two-dimensional system free from chemical disorder, and great starting conditions for realizing the QSL state. Indeed, the signature of forming a QSL state has been observed in AC susceptibility measurements of $PrZnAl_{11}O_{19}$ revealing no spin freezing or ordering down to 50 mK, despite a considerable antiferromagnetic coupling strength of about - 9 K. In addition, inelastic neutron scattering exhibits an abnormal broadening of low energy excitations at ~1.5 meV [13]. Unfortunately single crystals of $PrZnAl_{11}O_{19}$ are currently not available at the size needed for inelastic neutron scattering.

By substituting Zn with the less evaporative Mg element, we have succeeded in growing sizable single crystals of $PrMgAl_{11}O_{19}$ suitable for neutron scattering measurement. However, we have identified site disorder within the mirror plane, with about 7% of the Pr ions displaced from the ideal position. Magnetic susceptibility measurements show the moments lying perfectly along the *c*-axis (or perpendicular to the triangular plane) and do not freeze down to 50 mK. We argue that the system keeps fluctuating despite strong couplings and site disorder, which makes this system unique for a triangular system with Ising character.

1. Methods

Polycrystalline samples were prepared using a standard solid-state reaction technique. Raw materials of Pr_6O_{11} (99.99%), MgO (99.99%), and Al_2O_3 (99.99%) were dried at 900 °C over night prior to reaction to avoid moisture contamination. Then, stoichiometric amounts of the raw materials were mixed and ground thoroughly, pressed into pellets and sintered at 1400 °C ~ 1600 °C with several intermediate grindings. The powder sample was mixed with about 1% ~ 2% excess of MgO and pressed into a cylindrical rod of ~6 mm in diameter and ~140 mm (~35 mm) in length as a feed (seed) rod using a hydrostatic pressure of 70 MPa. The obtained feed and seed rods were sintered at 1500 °C for 2 h. Subsequent single crystal growth was conducted in an optical floating zone furnace (HKZ300) in pure argon atmosphere at 10 bar. After floating zone growth, the several-centimeter-sized as-grown crystal was annealed at 1000 °C in flowing O_2 for 24 h and then slowly cooled down to room temperature in order to avoid any possible oxygen vacancy.

The single crystal x-ray diffraction (XRD) measurement was performed on a XtaLAB Synergy diffractometer (Rigaku) at room temperature using the Mo-K_α radiation. The experimental conditions are tabulated in table 1. Part of the single crystal was crushed into powders for powder XRD measurement performed on a MiniFlex diffractometer (Rigaku) with

Table 1. Experimental conditions for the single crystal XRD measurements, and agreement factors for the refinement.

Formula	$PrMgAl_{11}O_{19}$
Space group	$P6_3/mmc$ (No. 194)
a, b (Å)	5.587 00(10)
c (Å)	21.8732(6)
V (Å^3)	591.29(2)
Z	2
2Θ (°)	3.72 - 82.16
No. of reflections, R_{int}	125 34, 4.11%
No. of independent reflections	614
No. of parameters	48
Index ranges	$-9 \leqslant H \leqslant 10,$ $-10 \leqslant K \leqslant 10,$ $-39 \leqslant L \leqslant 39$
R, wR_2 [a]	1.69%, 4.60%
Goodness of fit on F^2	1.42
Largest difference peak/hole (e/Å^3)	0.34/$-$0.38

[a] For a direct visualization of the fitting quality, see $F^2_{\text{obs.}}$ vs. $F^2_{\text{cal.}}$ in the SM [17].

the Cu-K_α radiation. JANA [15] and FULLPROF [16] packages were used for crystal structure refinement.

Heat capacity measurements were carried out on the Physical Property Measurement System (PPMS, Quantum Design) equipped with a dilution insert using the relaxation method. The DC magnetic susceptibility between 2 and 350 K was measured using the vibrating sample magnetometer (VSM) option of the PPMS. The AC magnetic susceptibility between 0.05 and 15 K was measured using the ACMS-II and ACDR options of the PPMS. For the AC susceptibility measurement, a driven field of 1–3 Oe in amplitude was used.

2. Results

The single crystal growth was initially attempted in a pure oxygen atmosphere, which turns out to be unstable and results in cavities along the as-grown crystals. This occurrence indicates the dissolution of oxygen in the melt, forming stable bubbles during the growth process. Therefore, subsequent growths were performed in a pure Ar atmosphere at 10 bar pressure in order to minimize the evaporation of the Mg element. The upper and lower rods were counter-rotated at a rate of 20 rpm, and moved downwards simultaneously at a rate of 2 mm h^{-1}. These conditions led to the successful growth of centimeter-sized single crystals, as depicted in the inset of figure 2(a). The single-domain nature was confirmed by Laue diffraction measurements along the rod. A typical Laue pattern is shown in figure 2(a) with the x-ray beam nearly parallel to the *c*-axis. Laue measurements also confirm that the crystal was grown along the a^* direction.

The quality of the single crystal was further characterized by x-ray diffraction of single crystals and crushed crystals. All peaks in the powder diffraction pattern can be indexed by

the space group $P6_3/mmc$, indicating an impurity-free phase; see the supplementary materials (SM) [17]. The precession images within the HK0, 0KL, and H0L planes from the single crystal XRD measurements are shown in figures 2(b)–(d). The sharp peaks confirm the high quality of the crystal. The structure refinement is consistent with the findings reported by Kahn *et al* for $LaMgAl_{11}O_{19}$ [11]. The final structure parameters extracted from the single crystal refinement are listed in table 2. It was found that about 7% of the Pr ions at the $2d$ (Pr1) site were shifted about 0.6 Å away from the ideal position towards the $6h$ (Pr2) site. Moreover, within the mirror plane of the structure, the Al5 ion displayed an anomalous atomic displacement parameter (ADP) along the *c*-axis, U_{33}, which amounts to 0.018 Å^2, compared to the others of around 0.007 Å^2. Therefore, it is set to be slightly off the mirror plane with half occupancy at the $4e$ site. Note, that with the resolution of our lab-based powder x-ray diffractometer, this anomalous ADP would be within errors and not highlighted. The last unsolved issue is the occupied position of the Mg ions. It is difficult to distinguish Mg^{2+} from Al^{3+} by means of x-ray diffraction because of the same number of electrons for both ions. However, neutron powder diffraction measurement on its sister compound $CeMgAl_{11}O_{19}$ [18] indicated that Mg is likely positioned at the Al3 site with an AlO_4 tetrahedron coordination, which also shows an anomalous ADP if solely occupied by Al ions. Therefore, the Mg ions are mixed with the Al3 ion at the $4f$ site with 0.5 occupancy. The refined structure is shown in figure 1 and those particular ions are highlighted.

Moving to the magnetic property measurements. The x-ray photoelectron spectroscopy (XPS) measurements indicate a pure Pr^{3+} state [17]. Figure 3(a) shows the temperature dependence of the magnetic susceptibility measured along different crystallographic directions. Note, that the *c*- and c^*-directions are identical. The data shows pronounced anisotropy behavior with the moment predominantly aligned along the *c*-axis. No difference between the zero-field-cooled (ZFC) and field-cooled (FC) curves can be observed, consistent with a dynamical (paramagnetic) state. The temperature dependence of χ_c^{-1} is shown in figure 3(b). A Curie–Weiss (CW) fit, $\chi_c^{-1} = (T - \theta_{\text{CW}})/C$, to the data above 250 K yields a positive Curie temperature θ_{CW} of 67 K. It should be noted that at these elevated temperatures we expect a large contribution from the crystal electric field (CEF) effect since two CEF levels were observed at ~12 and 35 meV [13] in the isostructural $PrZnAl_{11}O_{19}$. At low temperatures where only the low-lying CEF ground state is occupied, the influence from the higher excitation levels is negligible, a CW-like fit then provides a measure of the intersite interactions. A fit below 10 K yields θ_{CW} of -8 K, indicating strong antiferromagnetic couplings; see figure 3(b). The effective moment is 5.18 μ_B/Pr, which is close to the expected value of $g_c^{\text{ESR}}\sqrt{(S(S+1)} = 4.42\mu_B$/Pr, where $g_c^{\text{ESR}} = 5.1$ is the g factor determined from ESR measurement [17], and $S = 1/2$, implying that the low temperature magnetic properties are governed by an effective
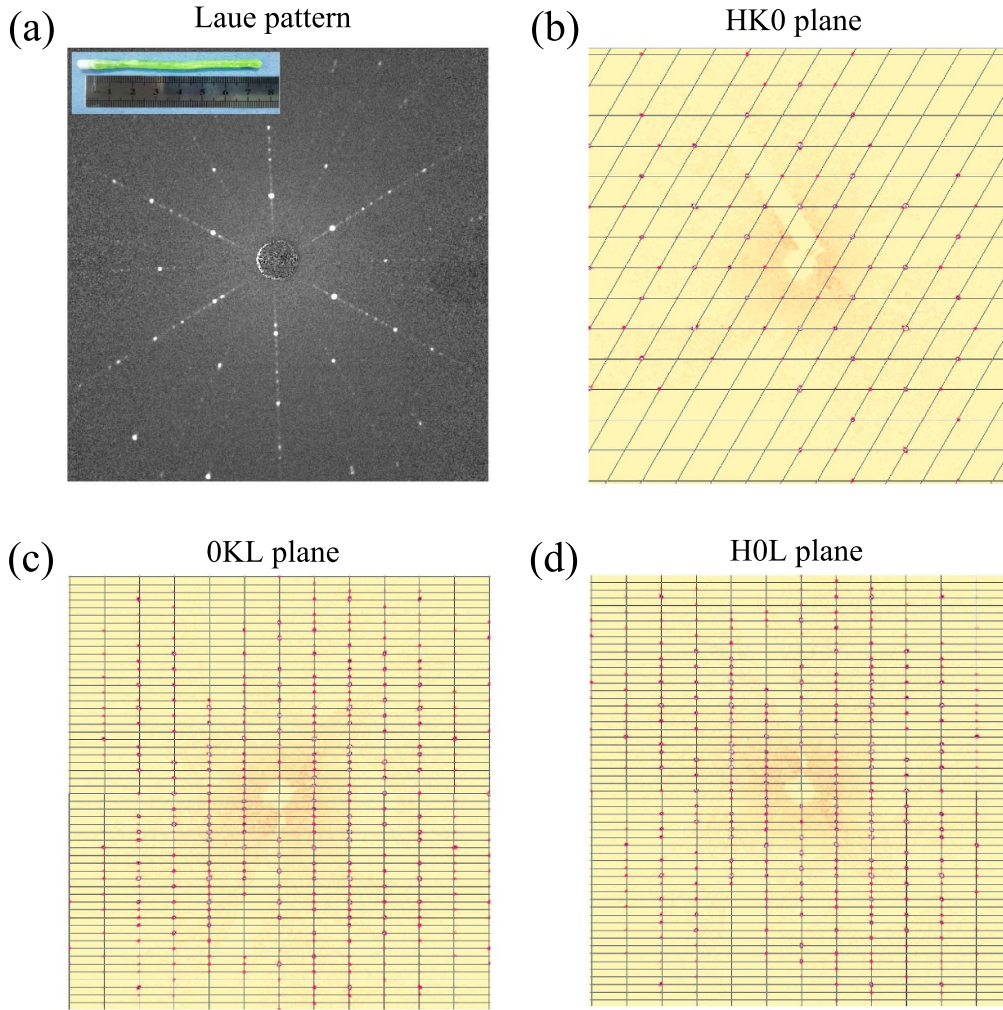
Figure 2. X-ray studies of PrMgAl$_{11}$O$_{19}$. (a) A Laue pattern with the x-ray beam approximately along the *c* axis. The inset shows a photo of the as-grown single crystal. (b)–(d) Precession images within the HK0, 0KL and H0L planes constructed from the single-crystal XRD measurements.

$S = 1/2$ state. AC susceptibility measurements along the *c*-axis show no sign of long-range ordering, nor any spin freezing down to 50 mK; see figure 3(c). The field dependence of isothermal magnetization (figure 3(d)) reveals negligible magnetization along the *a** direction compared to that of the *c* direction. It is about 20 times larger along the *c* axis at 2 K and 14 T, which can be easily explained by a slight misalignment (2 degrees) of the crystal during the measurement. Thus, the system can be considered as a well-defined Ising system.

In order to have more insights into the magnetic ground state, we performed CEF analysis and fit the CEF Hamiltonian to $\chi_c^{-1}(T)$. Although there are two inequivalent Pr sites, most of the Pr ions (>90%) are still located at the 2*d* site with a D_{3h} symmetry. Thus, we start with a model disregarding the disorder effect at the Pr site. In such a case, the CEF Hamiltonian can be expressed as

$$\mathscr{H}_{\text{CEF}} = \sum_{n,m} B_n^m O_n^m, \tag{1}$$

where O_n^m are the Stevens operators, and only the CEF parameters B_2^0, B_4^0, B_6^0 and B_6^6 are nonzero. The presence of the O_6^6 term admixes those states $|J, m_J\rangle$ differ in m_J by 6. For Pr^{3+}, the total angular momentum number $J = 4$. Thus, there are three doublets: two are formed by a linear combination of $|\pm 4\rangle$ and $|\mp 2\rangle$, and the other is $|\pm 1\rangle$. The three singlets are consisting of $|3^a\rangle = 1/\sqrt{2}(|3\rangle + |-3\rangle)$, $|3^b\rangle = 1/\sqrt{2}(|3\rangle - |-3\rangle)$, and $|0\rangle$. Therefore, if the ground state is a doublet and well separated from the first excited state, it will be highly anisotropic since $\langle J^\pm \rangle = 0$. To estimate the energy separation, we use the PyCrystalField package [19] to fit $\mathscr{H}_{\text{CEF}}$ to the magnetic susceptibility data. To do so, we calculate the magnetic susceptibility $\chi_{\text{CEF}}^c = M_{\text{CEF}}^c/H$ based on the CEF

Table 2. Refined crystal structure parameters.

Atom	occ.	x	y	z
Pr1 (2d)	0.928(10)	1/3	2/3	0.75
Pr2 (6 h)	0.024(3)	0.271(5)	0.729(5)	0.75
Al1 (2a)	1	0	0	0
Al2 (4f)	1	1/3	2/3	0.189 98(4)
Al3 (4f)	0.5	1/3	2/3	0.472 75(4)
Mg (4f)	0.5	1/3	2/3	0.472 75(4)
Al4 (12k)	1	0.167 38(4)	0.334 77(9)	0.608 39(2)
Al5 (4e)	0.5	0	0	0.2428(3)
O1 (6 h)	1	0.181 22(15)	0.3624(3)	0.25
O2 (12k)	1	0.152 14(11)	0.3043(2)	0.446 09(6)
O3 (12k)	1	−0.0112(2)	0.494 42(11)	0.348 08(5)
O4 (4f)	1	1/3	2/3	0.558 37(10)
O5 (4e)	1	0	0	0.348 18(9)

Atom	U_{11}/U_{12} (Å^2)	U_{22}/U_{13} (Å^2)	U_{33}/U_{23} (Å^2)
Pr1	0.0099(3)	0.0099(3)	0.007 56(13)
	0.004 93(15)	0	0
Pr2	0.030(5)	0.030(5)	0.019(4)
	0.007(5)	0	0
Al1	0.0070(3)	0.0070(3)	0.0078(5)
	0.003 52(14)	0	0
Al2	0.0072(2)	0.0072(2)	0.0067(4)
	0.003 58(11)	0	0
Al3/Mg	0.0068(2)	0.0068(2)	0.0076(4)
	0.003 40(12)	0	0
Al4	0.006 82(17)	0.0071(2)	0.0075(2)
	0.003 53(11)	−0.000 07(7)	−0.000 13(14)
Al5	0.0069(3)	0.0069(3)	0.018(3)
	0.003 47(17)	0	0
O1	0.0107(5)	0.0075(6)	0.0080(7)
	0.0038(3)	0	0
O2	0.0096(4)	0.0123(5)	0.0091(5)
	0.0062(2)	0.001 17(19)	0.0023(4)
O3	0.0079(4)	0.0077(3)	0.0086(5)
	0.0040(2)	0.0005(3)	0.000 24(17)
O4	0.0075(5)	0.0075(5)	0.0119(9)
	0.0037(2)	0	0
O5	0.0078(4)	0.0078(4)	0.0103(8)
	0.0039(2)	0	0

Hamiltonian, and treat the influence of the surrounding ions to a mean field level, so that $\chi_{\text{cal}}^c = \chi_{\text{CEF}}^c/(1 - \lambda\chi_{\text{CEF}}^c)$. By minimizing $\chi^2 = \sum_i (1/\chi_{\text{cal},i}^c - 1/\chi_{\text{obs},i}^c)^2$, the best fit yields $B_2^0 = -0.841\,81$ meV, $B_4^0 = -0.005\,16$ meV, $B_6^0 = -0.000\,12$ meV, $B_6^6 = -0.006\,02$ meV, and $\lambda = -1.19$ T/μ_B. The eigenvectors and eigenenergies can be found in the SM [17]. The negative λ indicates an antiferromagnetic interaction among the spins. From $\lambda = zJ_c/(\mu_B g_J)^2$, where z is the number of nearest neighbors, the exchange constant J_c can be estimated as $\sim -0.73\times10^{-2}$ meV (-0.08 K). The small exchange constant is partly due to the large effective moment of Pr^{3+} ($J = 4$) [20]. In the effective spin $S = 1/2$ picture, it will be enhanced by a factor of $\frac{J(J+1)}{S(S+1)} = 26.7$ (~ -2.1 K). Correspondingly,

the CW temperature at low temperature can be estimated as $\theta_{\text{CW}}^{\text{cal.}} = S(S+1)zJ_c/3k_B \sim$ -3 K, which is roughly consistent with the experimental value. The calculated $(\chi_{\text{cal}}^c)^{-1}$ is shown in figure 3(b), which reproduces the overall data very well. Using the CEF parameters and λ, the calculated isothermal magnetization is shown in figure 3(d). Again, the calculated curves agree well with the experimental values. The small discrepancy below ~10 K may suggest the onset of spin–spin interactions. Moreover, the g factors corresponding to the ground state doublets amount to $g_{ab} = g_J\langle\mp|J^{\mp}|\pm\rangle = 0$ and $g_c = 2g_J\langle\pm|J_z|\pm\rangle = 5.6$, consistent with the Ising character as inferred from the susceptibility measurements. The calculated g_c is also close to the ESR result [17]. These good agreements indicate that the magnetic ground state is well captured by our CEF analysis, although the excited state may be overestimated.

Figure 4(a) shows the specific heat measurements for PrMgAl$_{11}$O$_{19}$ under various magnetic fields. A nonmagnetic sample LaMgAl$_{11}$O$_{19}$ was also measured as a comparison. A broad hump can be observed at ~4 K in the zero field data. With an increase in magnetic field, the peak is shifted towards high temperatures, reminiscent of the Schottky anomaly. However, upon subtracting the phonon contributions using LaMgAl$_{11}$O$_{19}$ as a reference sample, the magnetic component, C_m, can be obtained and shown in figure 4(b). It is apparent that C_m of PrMgAl$_{11}$O$_{19}$ does not exhibit a typical (multi-level, broadened) Schottky behavior [21, 22], especially at the high temperature side where it displays a continuous increase up to 40 K. As a comparison, figure 4(d) shows the C_m of NdMgAl$_{11}$O$_{19}$ which displays the prototypical Schottky signature of a 2-level system. Along with the experimental data, a two-level Schottky fit, $C_m = p \cdot R(\frac{\Delta}{k_BT})^2 \frac{\exp(\Delta/k_BT)}{[1+\exp(\Delta/k_BT)]^2}$, where R is the ideal gas constant, Δ is the gap between the two levels, k_B is the Boltzmann's constant, and p represents the fraction of free ions [23] is depicted. In polycrystalline PrZnAl$_{11}$O$_{19}$, the C_m follows a power law in the temperature range between 0.2 and 2 K [13]. However in our PrMgAl$_{11}$O$_{19}$ data (figure 4(b)), C_m decreases faster than anticipated by a power law, suggesting the presence of a gap not seen in the Zn-analogue. On the other hand, the released entropy increases monotonically with increasing temperature, as shown in figure 4(c), in a similar manner to that seen in the polycrystalline PrZnAl$_{11}$O$_{19}$ sample [13].

3. Discussions

One essential discovery in the present study is the quenched disorder observed from single crystal x-ray diffraction refinements. The role of disorder in QSL is still elusive, and varies significantly from sample to sample. While it may drive a system into a glassy state, it may also enhance quantum fluctuations and potentially facilitate the formation of a QSL state, as demonstrated both theoretically and experimentally [3–5, 24]. The AC susceptibility data in figure 3(c) and the lack of
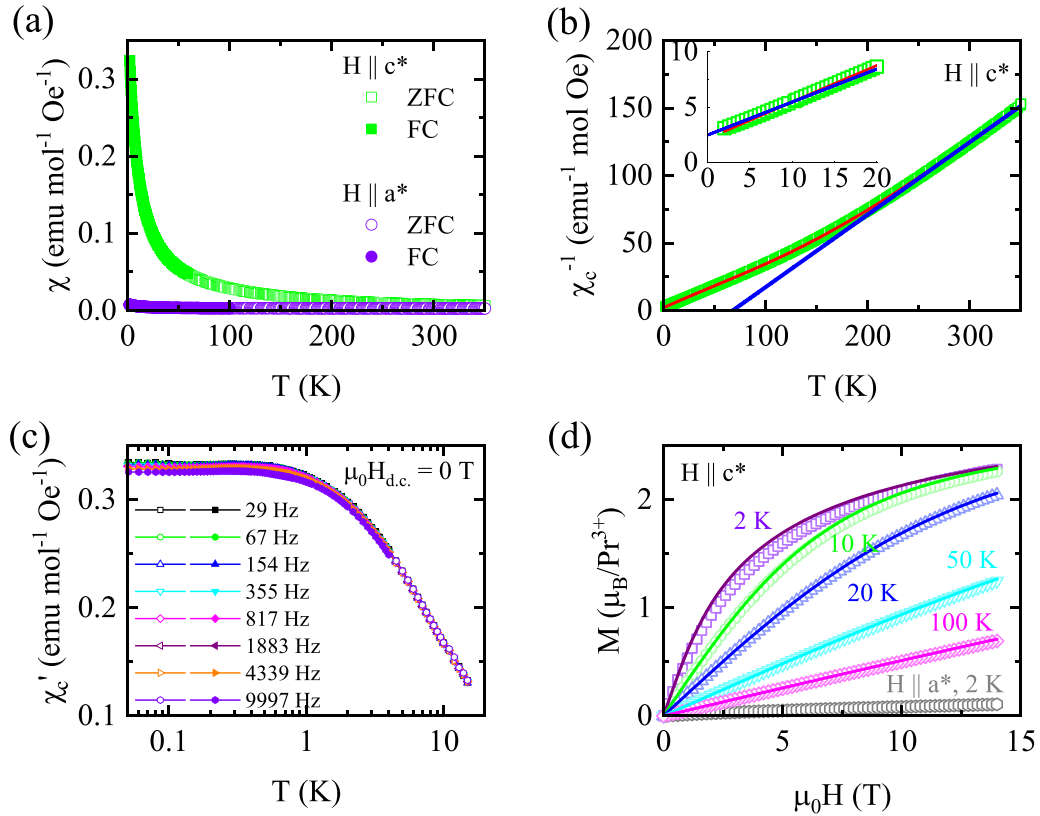
Figure 3. Temperature and field dependence of the dynamic susceptibility of $PrMgAl_{11}O_{19}$. (a) Temperature dependence of the magnetic susceptibility measured with the magnetic fields applied along the reciprocal a^* and c^* directions. (b) Temperature dependence of the inverse susceptibility, $\chi_c^{-1}(T)$. The red and blue curves are according to the CEF fit and Curie–Weiss fit, respectively. The inset highlights the low-temperature region. (c) Temperature dependence of the real component of the ac susceptibility, $\chi_c'(T)$, measured at various frequencies. (d) Isothermal magnetization measured at various temperatures. The solid lines represent the magnetization calculated from the CEF parameters.

frequency-dependent in the data down to 50 mK, indicate that the system is still dynamic even though there is measurable site disorder. One possible scenario is the strong fluctuations resulting from the geometric frustration of antiferromagnetically coupled, easy-axis spins on the triangular lattice cannot be relieved by the site disorder (~7%), which would intuitively result in the destruction of the spin liquid state. Alternatively, the site disorder may cooperate with the frustration and stabilize a spin-liquid-like state as proposed for $YbMgGaO_4$ [2, 25–29]. The present study does not have sufficient information to distinguish between these possibilities. Systematic studies on samples with different degrees of disorder will be instructive to clarify this point. Similar questions have been addressed in the pyrochlore oxide $Yb_2Ti_2O_7$, where a sharp peak in the specific heat for polycrystalline samples, due to a magnetic transition at ~265 mK [30], was not observed in many single crystals, where only a broad peak at lower temperature was observed [31, 32]. To investigate the small degree of site disorder found

here within powder samples will need higher spatial resolution measurements, such as neutron/x-ray pair distribution function (PDF) method and extended x-ray absorption fine structure (EXAFS) to illustrate the local structure differences.

Another prominent feature of $PrMgAl_{11}O_{19}$ is the distinct Ising anisotropy revealed by the magnetization measurements. While the Heisenberg model usually predicts a magnetically ordered state for a triangular antiferromagnet, the Ising model can result in a macroscopically degenerated spin liquid state [33]. Recent examples illustrating this concept is the $TmMgGaO_4$ [34–36] and neodymium heptatantalate, $NdTa_7O_{19}$ [37]. However, $TmMgGaO_4$ shows a partial order state below 0.7 K, and a lack of single crystals for $NdTa_7O_{19}$ hinders further explorations such as inelastic neutron scattering, as well as the exotic magnetic behaviors related to the crystalline directions. In this sense, the availability of large single crystals for $PrMgAl_{11}O_{19}$ provides a promising opportunity to investigate the triangular Ising model in depth.
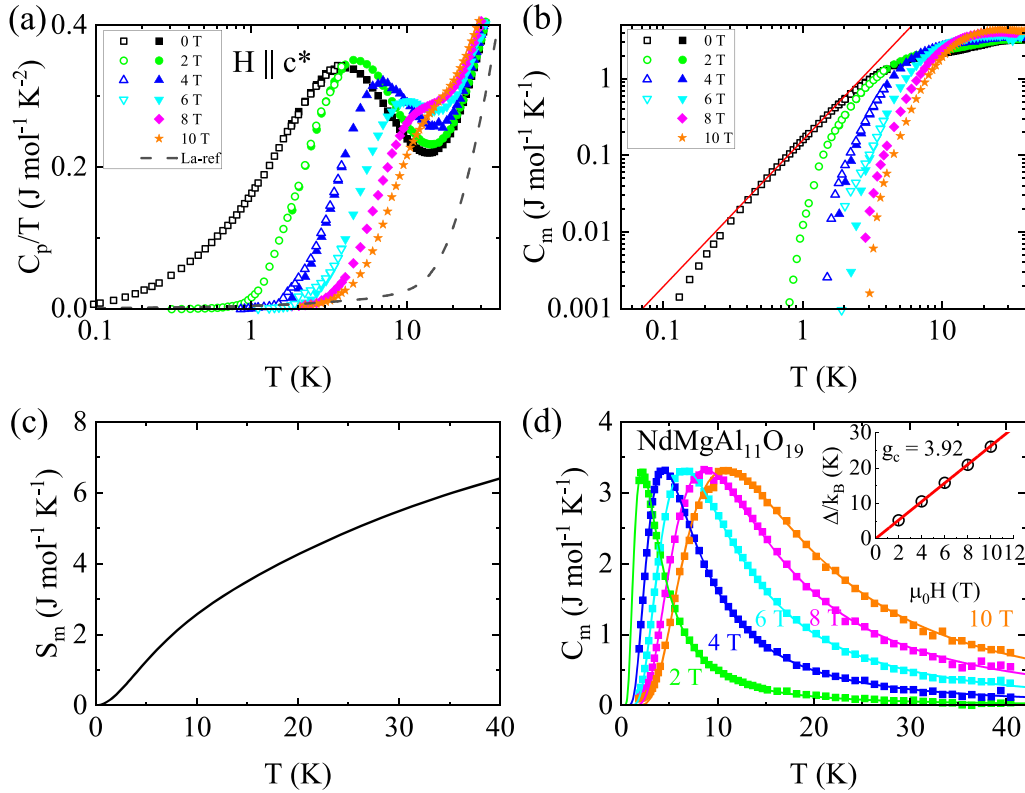
Figure 4. Heat capacity from hexaaluminate single crystals. (a) C_p/T versus T measured under various magnetic fields. The dashed line represents the phonon contribution obtained from the nonmagnetic counterpart $LaMgAl_{11}O_{19}$. (b) The magnetic specific heat is obtained by subtracting the phonon contributions ($LaMgAl_{11}O_{19}$) from the data of $PrMgAl_{11}O_{19}$. The red line represents a fit, $C_m = AT^\alpha$, to the zero field data in the temperature range between 0.2 and 2 K, with $\alpha = 1.91(1)$. (c) Representative change of the magnetic entropy in zero field. (d) Temperature dependence of the magnetic specific heat for $NdMgAl_{11}O_{19}$ together with a two-level Schottky fit. The inset shows the evolution of the gap as a function of the applied magnetic fields. A fit of $\Delta = g_c\mu_B H$ to the gap yields g_c of 3.92.

4. Conclusions

In summary, we have successfully synthesized centimeter-sized single crystals of a spin liquid candidate $PrMgAl_{11}O_{19}$ by means of the optical floating zone technique. Single crystal structure refinement unveiled the presence of about 7% quenched disorder at the Pr site in our sample. Directional magnetization measurements show a well-defined out-of-plane Ising anisotropy, which can induce strong fluctuations at a triangular lattice, as confirmed by the AC susceptibility measurements down to 50 mK. The availability of single crystals for this compound paves the way to explore the exotic magnetic properties by means of neutron scattering in the future.

While under review we became aware of a parallel work by Ma *et al*, who also conclude this sample is an Ising spin on the triangular lattice [38]. Here, by combining the CEF calculation, magnetization data and estimated *g*-factors by ESR results, we present more robust evidence on the Ising anisotropy. Moreover, without single crystal structure refinement, the disorder at the Pr site was not reported in that work.

5. Future perspectives

While disorder or defect is inevitable in real materials, many researchers endeavour to produce crystals as perfect as possible to obtain their intrinsic properties, allowing one to validate theoretical models. On the other hand, in recent years, it has been realized that disorder may result in exotic phases such spin-liquid-like random-singlet state. Unveiling the role of disorder systematically turns out to be as challenging as producing ideal crystals. In the title compound, the site disorder is within the triangular magnetic sublattice, which is unique compared to, e.g. $YbMgGaO_4$ where the site disorder occurs completely at the nonmagnetic site. By substituting Pr with another rare earth element, we expect to find evidence of different degrees of site disorder at the magnetic site (presumably this is also true when the nonmagnetic ions are substituted too), which will be helpful in future studies to manipulate the disorder in a controllable way. Substituting the rare-earth ion will also change the local spin character decorating the triangular lattice due to a change in the crystalline electric field scheme. This provides researchers with another tuning parameter for

the magnetism in these hexaaluminates and should result in the discovery of systems with the spins confined to the triangular plane or with more exotic spin textures. As with the magnetic pyrochlore oxides [39], the availability of large single crystals and the large number of chemical substitutions that present themselves, we envisage this avenue of research to be very fruitful, resulting in materials with a variety of properties including superconductivity, emergent quantum phenomena, exotic spin texture and other QSLs.

Acknowledgments

Author contributions

Conceptualization: H G, Z T; crystal growth: Y C and H G; measurement: Y C, H B, Z T and Z O; analysis: Y C and H G; validation: Z F, J S G, Z L, and J Z; writing: J S G Z T and H G with inputs from all authors. All authors have read and agreed to the published version of the manuscript.

Conflict of interest

The authors declare no conflict of interests.

ORCID iDs

Yantao Cao ⬤ https://orcid.org/0000-0003-1435-6932
Hanjie Guo ⬤ https://orcid.org/0000-0001-6203-5557

References

[1] Balents L 2010 Spin liquids in frustrated magnets *Nature* **464** 199

[2] Ma Z *et al* 2018 Spin-glass ground state in a triangular-lattice compound YbZnGaO$_4$ *Phys. Rev. Lett.* **120** 087201

[3] Savary L and Balents L 2017 Disorder-induced quantum spin liquid in spin ice pyrochlores *Phys. Rev. Lett.* **118** 087203

[4] Wen J-J *et al* 2017 Disordered route to the coulomb quantum spin liquid: random transverse fields on spin ice in Pr$_2$Zr$_2$O$_7$ *Phys. Rev. Lett.* **118** 107206

[5] Murayama H *et al* 2020 Effect of quenched disorder on the quantum spin liquid state of the triangular-lattice antiferromagnet 1T − TaS$_2$ *Phys. Rev. Res.* **2** 013099

[6] Gao Y and Chen G 2020 Some experimental schemes to identify quantum spin liquids *Chin. Phys. B* **29** 097501

[7] Knolle J and Moessner R 2019 A field guide to spin liquids *Annu. Rev. Condens. Matter Phys.* **10** 451–72

[8] Yamashita M *et al* 2010 Highly mobile gapless excitations in a two-dimensional candidate quantum spin liquid *Science* **328** 1246–8

[9] Ni J M *et al* 2019 Absence of magnetic thermal conductivity in the quantum spin liquid candidate EtMe$_3$Sb[Pd(dmit)$_2$]$_2$ *Phys. Rev. Lett.* **123** 247204

[10] Saber D, Dexpert-Ghys J, Caro P, Lejus A M and Vivien D 1985 Analysis and simulation of optical and magnetic properties of lanthanide aluminates LnMgAl$_{11}$O$_{19}$ (Ln = La/Nd,La/Eu,Pr) with magnetoplumbite-like structure *J. Chem. Phys.* **82** 5648–57

[11] Kahn A *et al* 1981 Preparation, structure, optical and magnetic properties of lanthanide aluminate single crystals (LnMAl$_{11}$O$_{19}$) *J. Appl. Phys.* **52** 6864–9

[12] Ashtar M *et al* 2019 REZnAl$_{11}$O$_{19}$ (RE = Pr, Nd, Sm - Tb): a new family of ideal 2D triangular lattice frustrated magnets *J. Mater. Chem.* C **7** 10073–81

[13] Bu H *et al* 2022 Gapless triangular-lattice spin-liquid candidate PrZnAl$_{11}$O$_{19}$ *Phys. Rev.* B **106** 134428

[14] Li Y 2019 YbMgGaO$_4$: a triangular-lattice quantum spin liquid candidate *Adv. Quantum Technol.* **2** 1900089

[15] Petříček V, Dušek M and Palatinus L 2014 Crystallographic computing system JANA2006: general features *Z. Kristallogr.* **229** 345–52

[16] Rodríguez-Carvajal J 1993 Recent advances in magnetic structure determination by neutron powder diffraction *Physica* B **192** 55–69

[17] See the supplementary materials

[18] Cao Y, Pomjakushin V, Gardner J S and Guo H Data to be published

[19] Scheie A 2021 PyCrystalField: software for calculation, analysis and fitting of crystal electric field Hamiltonians *J. Appl. Cryst.* **54** 356–62

[20] Scheie A, Garlea V O, Sanjeewa L D, Xing J and Sefat A S 2020 Crystal-field Hamiltonian and anisotropy in KErSe$_2$ and CsErSe$_2$ *Phys. Rev.* B **101** 144432

[21] Schotte K D and Schotte U 1975 Interpretation of kondo experiments in a magnetic field *Phys. Lett.* A **55** 38–40

[22] Bredl C D, Steglich F and Schotte K D 1978 Specific heat of concentrated kondo systems: (La, Ce)Al$_2$ and CeAl$_2$ *Z. Phys.* B **29** 327–40

[23] Gopal E 1966 *Sepcific Heats at Low Temperatures* (Plenum Press)

[24] Furukawa T *et al* 2015 Quantum spin liquid emerging from antiferromagnetic order by introducing disorder *Phys. Rev. Lett.* **115** 077001

[25] Kimchi I, Nahum A and Senthil T 2018 Valence bonds in random quantum magnets: theory and application to YbMgGaO$_4$ *Phys. Rev.* X **8** 031028

[26] Li Y *et al* 2019 Rearrangement of uncorrelated valence bonds evidenced by low-energy spin excitations in YbMgGaO$_4$ *Phys. Rev. Lett.* **122** 137201

[27] Wu H-Q, Gong S-S and Sheng D N 2019 Randomness-induced spin-liquid-like phase in the spin-$\frac{1}{2}$ $J_1 − J_2$ triangular heisenberg model *Phys. Rev.* B **99** 085141

[28] Ma Z *et al* 2021 Disorder-induced broadening of the spin waves in the triangular-lattice quantum spin liquid candidate YbZnGaO$_4$ *Phys. Rev.* B **104** 224433

[29] Li Y, Gegenwart P and Tsirlin A A 2020 Spin liquids in geometrically perfect triangular antiferromagnets *J. Phys.: Condens. Matter* **32** 224004

[30] Hodges J A *et al* 2002 First-order transition in the spin dynamics of geometrically frustrated Yb$_2$Ti$_2$O$_7$ *Phys. Rev. Lett.* **88** 077204

[31] Yaouanc A, Dalmas de Réotier P, Marin C and Glazkov V 2011 Single-crystal versus polycrystalline samples of magnetically frustrated Yb$_2$Ti$_2$O$_7$: specific heat results *Phys. Rev.* B **84** 172408

[32] Ross K A *et al* 2012 Lightly stuffed pyrochlore structure of single-crystalline $Yb_2Ti_2O_7$ grown by the optical floating zone technique *Phys. Rev.* B **86** 174424

[33] Wannier G H 1950 Antiferromagnetism. The triangular ising net *Phys. Rev.* **79** 357–64

[34] Shen Y *et al* 2019 Intertwined dipolar and multipolar order in the triangular-lattice magnet $TmMgGaO_4$ *Nat. Commun.* **10** 4530

[35] Li Y *et al* 2020 Partial up-up-down order with the continuously distributed order parameter in the triangular antiferromagnet $TmMgGaO_4$ *Phys. Rev.* X **10** 011007

[36] Li H *et al* 2020 Kosterlitz-thouless melting of magnetic order in the triangular quantum ising material $TmMgGaO_4$ *Nat. Commun.* **11** 1111

[37] Arh T *et al* 2022 The Ising triangular-lattice antiferromagnet neodymium heptatantalate as a quantum spin liquid candidate *Nat. Mater.* **21** 416–22

[38] Ma Z *et al* 2024 Possible gapless quantum spin liquid behavior in the triangular-lattice ising antiferromagnet $PrMgAl_{11}O_{19}$ *Phys. Rev.* B **109** 165143

[39] Gardner J S, Gingras M J P and Greedan J E 2010 Magnetic pyrochlore oxides *Rev. Mod. Phys.* **82** 53–107